Contact engineering for graphene nanoribbon devices (F)

View Online　　Export Citation　　CrossMark

Zafer Mutlu,[1,a)] (iD) Christina Dinh,[1] (iD) Gabriela Borin Barin,[2] (iD) Peter H. Jacobse,[3] (iD) Aravindh Kumar,[4] (iD)
Debanjan Polley,[5,6] (iD) Hanuman Singh,[5] (iD) Ziyi Wang,[3] (iD) Yuxuan Cosmi Lin,[7] (iD) Adam Schwartzberg,[8] (iD)
Michael F. Crommie,[3,9,10] (iD) Klaus Mullen,[11] (iD) Pascal Ruffieux,[2] (iD) Roman Fasel,[2,12] (iD) and Jeffrey Bokor[5,9] (iD)

AFFILIATIONS

[1]Department of Materials Science and Engineering, University of Arizona, Tucson, Arizona 85719, USA
[2]Empa, Swiss Federal Labs for Materials Science and Technology, Dübendorf, Switzerland
[3]Department of Physics, UC Berkeley, Berkeley, California 94720, USA
[4]Department of Electrical Engineering, Stanford University, Stanford, California 94305, USA
[5]Department of Electrical Engineering and Computer Sciences, UC Berkeley, Berkeley, California 94720, USA
[6]Department of Physics & Nanotechnology, SRM Institute of Science and Technology, Kattankulathur, Tamil Nadu 603203, India
[7]Department of Materials Science and Engineering, Texas A&M University, College Station, Texas 77840, USA
[8]Molecular Foundry, Lawrence Berkeley National Laboratory (LBNL), Berkeley, California 94720, USA
[9]Materials Sciences Division, Lawrence Berkeley National Laboratory, Berkeley, California 94720, USA
[10]Kavli Energy NanoSciences Institute at the University of California Berkeley and the Lawrence Berkeley National Laboratory, Berkeley, California 94720, USA
[11]Max Planck Institute for Polymer Research, Mainz, Germany
[12]Department of Chemistry, Biochemistry and Pharmaceutical Sciences, University of Bern, Bern, Switzerland

[a)]Author to whom correspondence should be addressed: zmutlu@arizona.edu

ABSTRACT

Graphene nanoribbons (GNRs), when synthesized with atomic precision by bottom–up chemical approaches, possess tunable electronic structure, and high theoretical mobility, conductivity, and heat dissipation capabilities, which makes them an excellent candidate for channel material in post-silicon transistors. Despite their immense potential, achieving highly transparent contacts for efficient charge transport—which requires proper contact selection and a deep understanding of the complex one-dimensional GNR channel-three-dimensional metal contact interface—remains a challenge. In this study, we investigated the impact of different electron-beam deposited contact metals—the commonly used palladium (Pd) and softer metal indium (In)—on the structural properties and field-effect transistor performance of semiconducting nine-atom wide armchair GNRs. The performance and integrity of the GNR channel material were studied by means of a comprehensive Raman spectroscopy analysis, scanning tunneling microscopy (STM) imaging, optical absorption calculations, and transport measurements. We found that, compared to Pd, In contacts facilitate favorable Ohmic-like transport because of the reduction of interface defects, while the edge structure quality of GNR channel plays a more dominant role in determining the overall device performance. Our study provides a blueprint for improving device performance through contact engineering and material quality enhancements in emerging GNR-based technology.

Published under an exclusive license by AIP Publishing. https://doi.org/10.1063/5.0172432

I. INTRODUCTION

Historically, improvements in logic computing performance have been maintained by miniaturizing silicon transistors at a pace given by Moore's famous law.[1] This progress has been facilitated by innovations like strained silicon, high dielectric constant materials, and FinFET structures. However, as technology continues to advance, the semiconductor industry faces significant fundamental challenges, including

quantum tunneling, short-channel effects, and heat dissipation. To enable further scaling and advancements in computing power, it is essential to explore new transistor channel materials, innovative transistor structures, and device architectures.

Carbon nanotubes (CNTs) have been envisioned and studied as one of the most promising transistor channel candidates over two decades due to their remarkable electrical properties, but achieving high

24 October 2024 08:40:46

purity semiconducting CNTs remains one of the fundamental challenges.[2] As potential alternatives to CNTs, bottom–up synthesized graphene nanoribbons (GNRs) possess high purity levels, thanks to their deterministic growth.[3] Theoretically, GNRs are expected to have excellent electrical properties similar to CNTs, particularly high intrinsic charge carrier mobility[4] and high on-state drive current.[5] Additionally, GNRs offer highly tunable bandgaps through their widths and topologies.[6,7] Combined with their high purity, these properties make GNRs highly promising candidates for transistor channels, particularly in high-performance logic applications. Nevertheless, the performance of GNR devices so far has been relatively poor,[8] and only a handful of studies have focused on exploring ways to improve their performance.[5,9–17]

A key factor in achieving high-performance GNR transistors is establishing a low-resistive interface between metal contacts and GNR channel. Currently, the best performance in GNR devices has been demonstrated using palladium (Pd) contacts.[5,14,18,19] Pd has also been successfully applied to carbon nanotube (CNT) devices.[20,21] However, GNR devices with Pd contacts still exhibit poor charge transport due to the formation of highly resistive contacts, resulting in electrical performance levels significantly below their theoretical values.[5] One potential explanation for the formation of this highly resistive contact might be the damage that occurred in the GNRs during the metal deposition process.[22–24] Given that GNRs are incredibly thin (comprising only one atom in thickness), it is not unreasonable to think that Pd—with its high vapor pressure, melting point, and chemical reactivity—could cause damage to GNRs. This damage results in a defective interface that restricts the flow of charge carriers to/from GNR channel.

One promising approach to improve the metal–contact interface is to utilize softer metal contacts such as indium (In) or tin (Sn).[22–24] These metals, particularly In, have been shown to be compatible with two-dimensional (2D) materials such as monolayer/thin film MoS_2, WSe_2, WS_2, and NbS_2 and have been shown to establish van der Waals (vdWs) interfaces and Ohmic-like transport behavior.[22–24] Given that GNRs—being one-dimensional (1D) materials—share the natural thinness of these 2D materials in terms of being naturally thin, it is conceivable that employing these metals to fabricate contacts can minimize defect formation and result in cleaner interfaces, leading to improved performance.

In this study, we investigated the impact of Pd and In contacts on the electrical characteristics of semiconductor nine-atom-wide armchair-type GNR (9-AGNR) back-gated (BG) field-effect transistors (FETs) with varying source (S)-to-drain (D) spacing. The results indicate that In contacts promote favorable Ohmic-like transport, attributed to the reduced damage to the structural quality of the GNRs, compared to the case of Pd. We then discuss the importance of improving synthesis methods to ensure high structural quality for achieving optimal device performance.

II. RESULTS AND DISCUSSION

The synthesis of 9-AGNRs was performed on Au(111)/mica substrates from 3,6-diiodo-1,1:2,1-terphenyl (DITP) precursor using the established on-surface synthesis protocol.[25,26] This method was initially reported for the synthesis of 7-AGNRs by Cai *et al.*[3] and has been widely adopted for the synthesis of other GNRs.[27–37] The growth of 9-AGNRs, initially reported by Talirz *et al.*[25] using a bromine (Br)-based precursor, was later improved by employing an iodine (I)-based

precursor,[26] leading to improved GNR length. As shown in Fig. 1(a), the reaction proceeds in two sequential annealing steps involving an Ullmann-type polymerization reaction at $T_1 = 200\,°C$ and a subsequent cyclodehydrogenation (CDH) at $T_2 = 400\,°C$. Enabled by the flat surfaces of mica substrates, deposited atomically smooth Au(111) thin films serve as a catalyst for both chemical reactions and allow scanning tunneling microscopy (STM) analysis. Au(111) on mica substrates furthermore facilitate the transfer of GNRs onto dielectric substrates for device fabrication employing wet-etch methods developed for them.[5,8,38]

Figure 1(b) shows a representative scanning tunneling microscope (STM) image of a sample containing 9-armchair graphene nanoribbons (9-AGNRs) synthesized on Au(111) on mica at 1 monolayer coverage. The image reveals highly uniform and densely packed GNRs, with an average length ranging from 45 to 50 nm. Figure 1(c) shows a non-contact atomic force microscopy (nc-AFM) image capturing an individual 9-AGNR, revealing the well-defined width and edge topology along and on the GNR termini. The width of the GNRs measures approximately 0.95 nm. Theoretical calculations suggest that the free-standing 9-AGNR possesses a predicted bandgap of 2.29 eV, whereas the gold-supported 9-AGNR exhibits a bandgap of 1.4 eV.[39]

To investigate the impact of contact metal depositions on the GNRs, we first transferred two GNR samples onto pre-patterned SiO_2/Si chips with dimensions of $1 \times 1\,cm^2$. These chips contained BG devices with ~ 8 nm tungsten (W) gate metal capped with a ~ 5 nm hafnium dioxide (HfO_2) dielectric layer fabricated by atomic layer

(a)

(b)

(c)
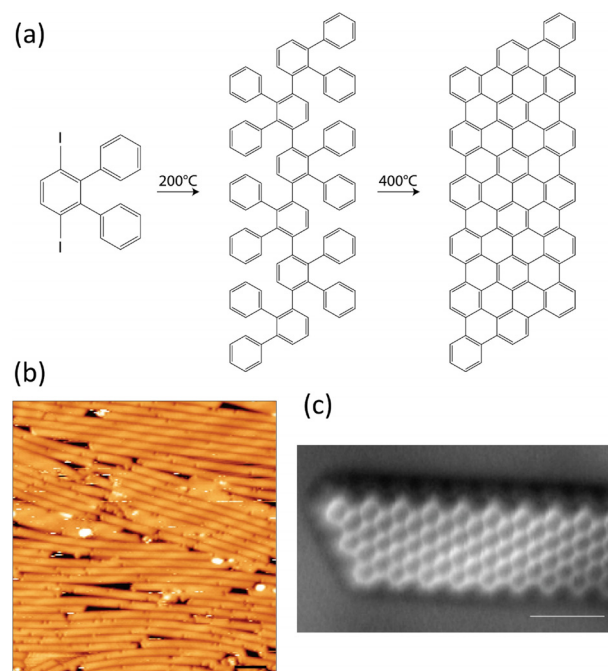
FIG. 1. On-surface synthesis of 9-AGNRs. (a) On-surface synthesis route for the growth of 9-AGNRs on an Au(111) surface from $3',6'$-diiodo-$1,1':2',1''$-terphenyl (DITP) precursor by two sequential annealing steps. (b) STM topographic scan ($V = -1.5$ V, $I = 30$ pA) of a 1 monolayer-coverage sample of 9-AGNRs on Au (111) on mica. The scale bar is 5 nm. (c) nc-AFM image of a 9-AGNR. The scale bar is 1 nm.

deposition (ALD). The transfer process was carried out using the polymer-free method reported in our previous work.[5]

Raman spectroscopy was utilized to corroborate growth and assess the quality of the GNRs, as well as to evaluate their structural integrity after transfer. The measurements were performed following the growth of 9-AGNRs on the Au(111) substrate and their subsequent transfer to the devices. In identical fashion to previous studies,[38,40] we employed a 785-nm wavelength laser. The photon energy of this laser closely matches the optical transition energy of 9-AGNRs,[41] resulting in a high Raman intensity.

Figure 2(a) shows a comparison of Raman spectra acquired on the as-grown 9-AGNRs on the Au(111) substrate and on the transferred GNRs on the device. Let us begin by discussing the Raman spectrum of the as-grown GNRs. The spectrum exhibits all the characteristic peaks of 9-AGNRs.[9] The G peak arises from C–C bond vibrations along the ribbon axis,[3] and its shape, location, and intensity can vary depending on the growth substrate type, crystallinity, and doping.[42–44] The D peak corresponds to the ring breathing mode of sp^2 atoms, resembling that of graphene.[45] Unlike graphene, where the D band excitation is only activated in the presence of defects, 9-AGNRs exhibit a D peak even in the absence of defects due to their edges. An additional peak associated with the theoretically predicted in-plane C–H bending modes localized along the edges[46,47] is observed in proximity to the D peak. In the low-frequency region, a radial-breathing like (RBLM) peak is present, analogous to the radial-breathing mode (RBM) observed in CNTs.[48,49] The presence of RBLMs serves as a distinctive characteristic of GNRs and provides valuable structural information.[50] The existence of these characteristic peaks with sharp features verifies the high quality of the GNRs.[51] Furthermore, the Raman spectrum, generated from a focal spot covering tens of thousands of nanoribbons, exhibits only one sharp and intense RBLM peak, confirming the width uniformity of virtually all GNRs. This uniformity is highly desirable for large-scale high-density transistor applications of GNRs in logic devices.

Moving on to the Raman spectrum of the transferred GNRs, the result indicates that all characteristic peaks of 9-AGNRs are preserved with similar intensities and shifts. The well-preserved GNR Raman features, along with the absence of C–O and O–H peaks, suggest that the GNRs remain structurally intact after transfer and are not damaged or chemically altered during the transfer process.[38,52]

After transferring the GNRs, we deposited a ~12 nm thick Pd film on one half of the sample. On the other half of the same sample, we deposited two consecutive layers: an ~8 nm thick In film followed by a ~20 nm thick Au film. These depositions were carried out using e-beam deposition under high-vacuum conditions $p \sim 10^{-8}$ Torr. The choice of a ~12 nm Pd film for the GNR contacts follows the convention for GNRFETs, which has shown the best performance to date.[5,9,14,18,19] Regarding In contacts, we did not deposit a ~12 nm In layer due to the requirement of protecting In from oxidation in ambient conditions. In contacts typically require capping with either Au or Pd to prevent oxidation.[22–24] Considering that we aimed to build devices with small S-to-D gaps down to ~30 nm due to the average length of the GNRs (45–50 nm), the total electrode thickness needed to be limited to ~30 nm, explaining our choice of ~8 nm In and ~20 nm Au. These proportions were also used in a recent work on MoS_2.[23] The difference in thickness between In and Pd contacts does not pose a comparison problem because their resistivities are similar, regardless of thickness, and they both make uniform contact with GNRs. Additionally, the Au film does not alloy with In and does not impact electrical performance.
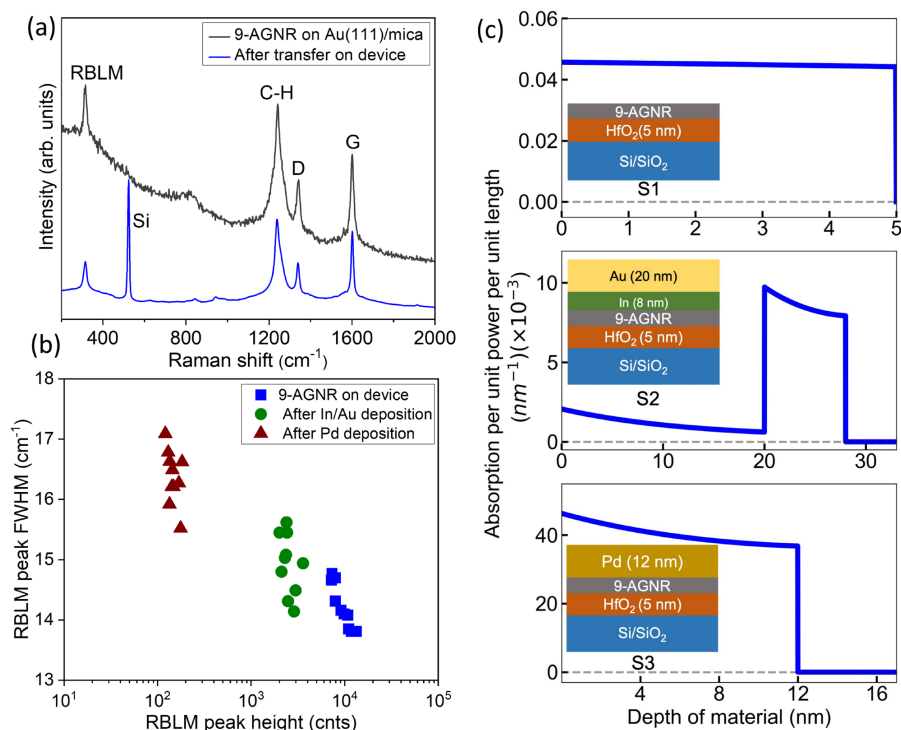

FIG. 2. Raman spectroscopy analysis of 9-AGNRs. (a) Raman spectrum of 9-AGNRs synthesized on the Au(111)/mica substrate and after transfer onto the local BG substrate. The laser excitation wavelength used is 785 nm. (b) Comparison of RBLM peak intensities and FWHM values of the as-transferred 9-AGNRs, after In/Au and Pd deposition. Data were collected from at least ten points from each sample. (c) Absorption profile (absorption per unit incident optical power per nm length) is calculated using the transfer matrix mechanism for the three samples (S1, S2, and S3) and plotted with the thickness of the structures. The schematic of each sample is given in the inset of the respective figures.

The Raman spectroscopy analysis in Fig. 2(b) shows noticeable differences in intensities and linewidth full-width half-maxima (FWHMs) of the RBLM of the GNRs between Pd and In/Au deposition. Pd deposition results in a broader linewidth and a significant reduction in the RBLM peak intensity compared to In/Au deposition. The width of the RBLM peak can be associated with the formation of defects,[51] and therefore the wider RBLM peak in the Raman spectrum after Pd deposition compared to that in In deposition suggests that more defects are induced after Pd deposition than after In deposition. Indeed, the introduction of these imperfections is primarily attributed to the high vapor pressure[53] and high melting temperature of Pd, which lead to high energies for Pd atoms and clusters. Furthermore, when combined with Pd's strong chemical reactivity,[54] this highly energetic Pd has the potential to cause disruptions in the GNR structure. On the other hand, In contacts shows a narrower RBLM peak, suggesting a more uniform and well-defined GNR structure with potentially less defects. In, with its low vapor pressure,[53] melting temperature, and chemical reactivity, is less likely to cause disruptions to the GNR structure during deposition. We observe that the RBLM peak intensity gets significantly reduced in sample S3 (sample containing 12 nm Pd) compared to the pristine sample (S1) and S2 (sample containing 20 nm Au/8 nm In) in Fig. 2(b). The peak intensity can, of course, be reduced due to quality of 9-AGNRs in these two samples. Now, we also know that Raman intensity is fundamentally a linear function of the incident (or available) optical power.[55] Due to the multilayer nature of the samples (S1, S2, and S3), the laser power gets absorbed differently in each layer depending on their thickness and optical constants. The total absorption can be calculated by solving the transfer matrix for each sample.[56,57] Hence, the available optical power for Raman scattering in the GNR layer might be different, which can, in principle, lead to the observed Raman peak intensity difference.

In Fig. 2(c), we have plotted the calculated absorption profile (i.e., absorption per unit incident optical power per nm depth of the sample) for the three different structures. The area under the curve [in Fig. 2(c)] is the total absorbed optical power (per unit incident optical power per unit area) in the sample. The smaller the absorption, the larger is the optical power available for Raman scattering by the GNRs in each sample and vice versa. Due to the absence of any metallic layers in S1, the calculated absorption is minimal; consequently, we experimentally observe a large Raman peak intensity [blue rectangles in Fig. 2(b)]. The optical absorption increases for both S2 and S3 due to the presence of thick metallic layers, and experimentally we observe reduced Raman peak intensity. However, the absorption is ~5 times larger in S3 compared to S2, which cannot explain the experimentally observed two orders of magnitude reduction in the Raman peak intensity (assuming the Raman peak intensity depends mostly on the available optical power for GNRs in each sample). The experimentally observed results in Fig. 2(b) indicate that the difference in the optical power alone cannot explain the large Raman intensity reduction in S3. Therefore, we conclude that the introduction of Pd contacts must lead to a deterioration in the GNR quality, which in turn results in the significant Raman intensity reduction.

Having established an understanding of the structural defect formation in GNRs upon Pd and In deposition, we now move on to a study of their electrical properties. To this end, we fabricated devices with Pd and In/Au contacts with similar thicknesses as in our Raman studies. A cross-sectional diagram of BG 9-AGNR devices is shown in
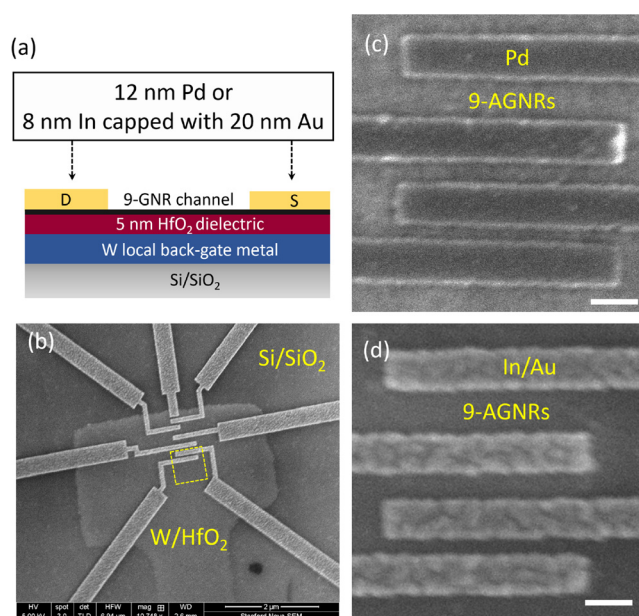
FIG. 3. Fabrication of 9-AGNR FETs. (a) Schematic of 9-AGNR FETs made with ~12 nm Pd or ~8 nm In capped with ~20 nm Au contacts deposited by e-beam deposition under similar experimental conditions. The device is made on a local back-gate geometry for better electrostatic control using an ultrathin ~5 nm ALD-grown HfO$_2$ gate dielectric and ~8 nm W metal deposited by the sputtering method. The devices were made using standard photolithography patterning, deposition, etching, and liftoff. The GNRs are wet-transferred onto the pre-patterned devices. After transferring the devices, the small metal contacts are made using EBL. (b) Low-magnification SEM image of the as-fabricated 9-AGNR FETs with different channel lengths. High-magnification SEM images of the electrodes made with Pd (c) and In/Au (d). The scale bars are 100 nm.

Fig. 3(a). The GNRs were successfully transferred to pre-patterned devices following the polymer-free transfer protocol. After the transfer, S and D electrodes with varying channel widths (W) and lengths (L) were patterned using the e-beam lithography (EBL) process, which involves e-beam writing, followed by e-beam deposition of metal and subsequent liftoff steps. A top-view low-magnification scanning electron microscopy (SEM) image of the fabricated device is shown in Fig. 3(b). High-resolution SEM images of Pd and In/Au contacts are presented in Figs. 3(c) and 3(d), respectively. While the SEM images show a slightly granular structure for In/Au contacts, electrical resistivity measurements indicate a comparable resistivity between both In/Au and Pd.

Figure 4 shows the electrical transport characteristics of the as-fabricated 9-AGNR FETs with Pd and In/Au contacts. When comparing the transfer characteristics (drain current I_D as a function of gate voltage V_{GS}) of the 9-GNR devices made with Pd and In/Au contacts, it can readily be seen that both devices exhibit a predominant p-type FET behavior [Fig. 4(a)]. The p-type behavior in the device with Pd contacts can be partially attributed to Pd's high work function.[8] However, the fact that the devices with low work function In contacts also show p-type transport suggests that there are other factors contributing to the observed p-type behavior. We note that both devices exhibit a positive shift in their transfer curves [Fig. 4(a)], possibly due to charge trapping in the dielectric layer and/or around the GNR
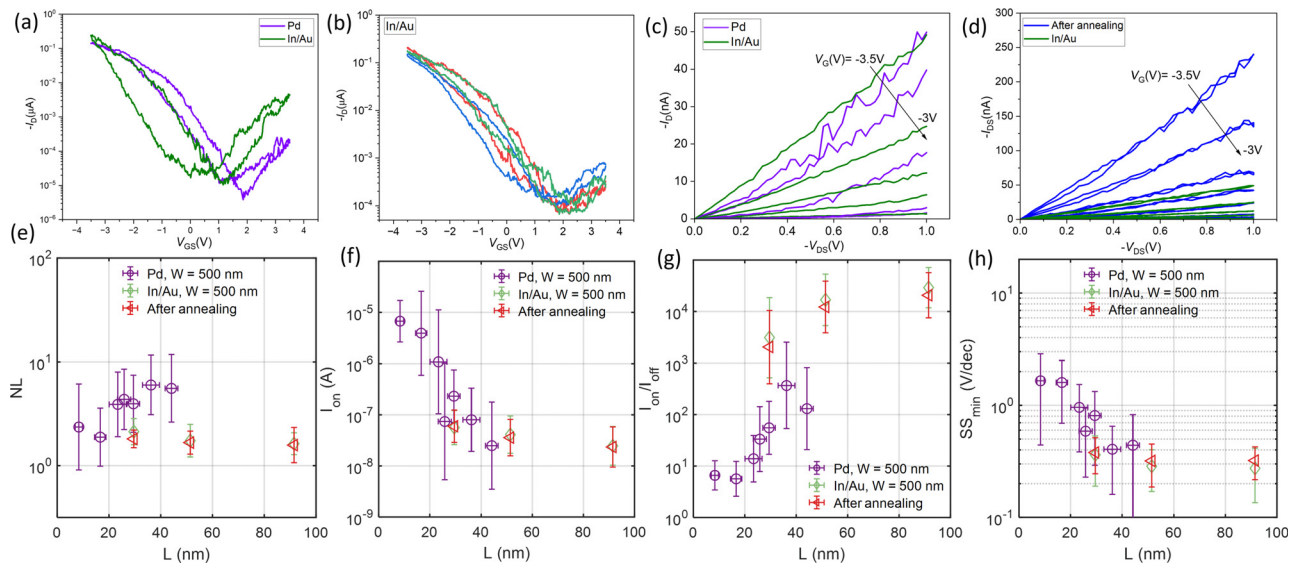
FIG. 4. Electrical transport characterization of 9-AGNR FETs. (a) Comparison of typical I_D–V_{GS} characteristics of 9-AGNR FETs with Pd and In/Au contacts. (b) I_D–V_{GS} characteristics of three different 9-AGNR FETs with In/Au contacts. (c) Comparison of typical I_D–V_{DS} characteristics of 9-AGNR FETs with Pd and In/Au contacts. (d) Comparison of I_D–V_{DS} characteristics of 9-AGNR FETs In/Au contacts before and after annealing. The device dimensions are W = 500 nm and L = 30 nm in (a)–(d). L dependence and comparison of NL (e), I_{on} (f), I_{on}/I_{off} (g), and SS_{min} (h) for devices made with In (in green) and Pd (in purple) contacts, with the inclusion of annealing data for In devices (in red). All measurements were conducted with a V_{DS} of −1 V, and the values of the I_{on} were recorded at a (V_{GS}) of −3.5 V. The I_{off} was taken when the drain current reached its minimum value.

channel. Assessing the symmetry of the devices would require applying larger positive voltages to compensate for these trapped charges, but this is not feasible because the ultrathin HfO_2 gate dielectric breaks down at voltages exceeding 3.5 V. The devices with both Pd and In/Au contacts exhibit similar electrical performance, with an on-current (I_{on}) of ∼ 0.1 μA and an on and off-current ratio (I_{on}/I_{off}) of ∼ 10^4. Assuming around ∼20 GNRs facilitate the current in the channel, the device yields a GNR-width normalized current drive of approximately 5.3 μA/μm for a width of 0.95 nm. It is noteworthy that the 9-aGNRs possess a larger bandgap of roughly 2.3 eV, so utilizing GNRs with a lower bandgap is anticipated to significantly reduce Schottky barrier (SB) and improve the device's performance.[58] Additionally, while the devices made with Pd contacts with L < 30 nm have the potential to exhibit >1 μA per ribbon and >25 μA per GNRFET device,[5,9,18] the present work utilizes only down to L = ∼30 nm. This conservative value was chosen to account for the unknown nature of In/Au deposition process. However, it is believed that devices with smaller L will perform even better, as the number of ribbons bridging the S and D increases significantly with decreasing L.[18] Figure 4(b) shows the I_D–V_{GS} characteristics of three devices fabricated with In/Au contacts and L = ∼30 nm. All devices exhibit hysteresis, similar to the behavior observed in Pd devices [see Fig. 4(a)]. Hysteresis has also been observed in the 2D materials,[59–61] and is attributed to the trapped charges located on the surface of the channel, within the gate dielectric, at the channel/dielectric interface, or within the channel itself.

Figure 4(c) shows the typical output characteristics (I_D vs source voltage V_{DS}) of the same devices, respectively. The I_D–V_{DS} curve for the devices with Pd contacts exhibit distinctly nonlinear behavior, suggesting a significant SB tunneling resistance at the GNR-contact.[8,18] On the other hand, the I_D–V_{DS} curve for the device with In/Au contact

at the same device dimensions shows a nearly linear response, suggesting a better metal contact. To quantitatively analyze the nearly linear response, we define the nonlinearity (NL) as

$$NL = \frac{I_D(V_{DS} = -1V)}{10 I_D(V_{DS} = -0.1V)}.$$

The average NL values for the devices with Pd and In/Au contacts with various Ls but the same W of 500 nm are plotted in Fig. 4(e). Remarkably, the device with In/Au contacts consistently exhibits lower NL values compared to the device with Pd contacts for the same L. These results indicate that the contact–GNR channel interface is improved with In. We, therefore, conclude that, compared to Pd, In introduces fewer defects that cause scattering and decrease the electrical performance.

Figures 4(f)–4(h) show the quantitative analysis of I_{on}, I_{on}/I_{off}, and subthreshold swing (SS_{min}) for devices fabricated with In and Pd contacts. The analysis shows that while no substantial improvements were observed in I_{on} and SS_{min}, In-based devices consistently showed higher I_{on}/I_{off} values, indicating superior performance compared to Pd-based devices. Moreover, In-based devices exhibited significantly smaller variation with lower error bars. Conversely, Pd-based devices showed greater variability, likely attributable to random damage in the GNRs, resulting in fluctuations in device parameters.

It is worthwhile to mention that since the GNRs randomly grow on Au(111)/mica substrates, after transfer, they randomly stay on the surface of pre-patterned devices. In order to establish functional GNR devices with desirable on-state current and on/off ratio characteristics, a fundamental requirement is that at least one GNR forms a continuous bridge from the S to the D electrodes, effectively establishing a

conductive path between them.[9] Given that the electrode widths measure 500 nm, our previous statistic calculations[18] suggest that there are several GNRs within the device structure with the potential to span and connect these electrodes. However, it is important to note that, due to the 100 nm width of the metal leads, the likelihood of a single GNR bridging more than one gap is almost zero, as the maximum length of a GNR is about 120 nm. Thus, only the GNR bridging has a dominant effect on the overall conductance, and any parasitic pathways should not significantly influence our results. There might be some network effect that may exist; however, we believe its impact to be minimal. Even if considering the contributions from the parasitic effects as well as network behaviors, since we are comparing Pd and In/Au contacted devices with the same geometry, this should not pose any comparison problem. Although it is not within the scope of this work, in future studies, we will investigate such effects.

To explore the possibility of further improving device performance, we annealed In devices fabricated in vacuum at $T = 250\,^\circ$C. Figures 4(e)–4(h) show that key device parameters remained similar after annealing. The mild annealing temperature is not expected to be sufficient to alloy In and Au and, therefore, no changes in the work function should take place, explaining the lack of changes to the device parameters.[24] On the other hand, the absence of degradation in device performance after annealing and presence of the linear I_D–V_{DS} behavior [Fig. 4(d)] is further evidence for the stability of In contacts. This stability is an important characteristic that ensures the reliability and durability of the devices over extended periods of operation.

While we have concrete evidence that the contact–GNR interface was improved, the lack of substantial device performance improvement, particularly in on-state current performance, indicates that the GNR channel material might have issues with charge transport. A likely explanation for the limited performance is the presence of "bite defects" (see the inset of Fig. 5 for the schematic of the defects) in the GNR channel, characterized by missing benzene rings at the edges, resulting in the scattering of charge carriers and a resulting decrease in charge transport through the channel.[62,63] To systematically study the bite defects, we obtained a high-resolution STM image of 9-AGNRs grown on Au(111)/mica substrate at low coverage, shown in Fig. 5(a), and performed a statistical distribution analysis of the defects along the lengths of the GNRs. Figure 5(b) shows the cumulative number of bite defects as a function of length x over all GNRs of Fig. 5(a). A linear fit to the data reveals that the defect density is roughly one defect for every 4 nm of 9-AGNRs, and therefore a GNR spanning a channel with L = 20 nm will be host to an average of five defects. Bite defects in 9-AGNRs are associated with a reduction in transmission on the order of roughly 30% to 50% as a result of scattering of charge carriers.[62,63] Therefore, even a conservative estimate of the reduction of current through a GNR spanning the channel is $\Delta G = G_0(1 - (1/2)^5) \approx 97\%$. Based on this finding, we recognize the importance of improving the quality of the channel in addition to optimizing the contact resistance between the metal contacts and the channel. Strategies to improve the GNR's inherent performance may include using GNRs that are less prone to the formation of bite defects or other defects that may induce scattering. For example, new types of GNRs with mixed armchair and zigzag edges are actively being explored, and some of them show promising electronic characteristics in addition to high atomic perfection.[64,65] Alternatively, alternative GNR structures may be used, which are less affected by defects in their transport. Examples of the latter category of GNRs are AGNRs with widths of 17 atoms,[66] or even wider.[62]
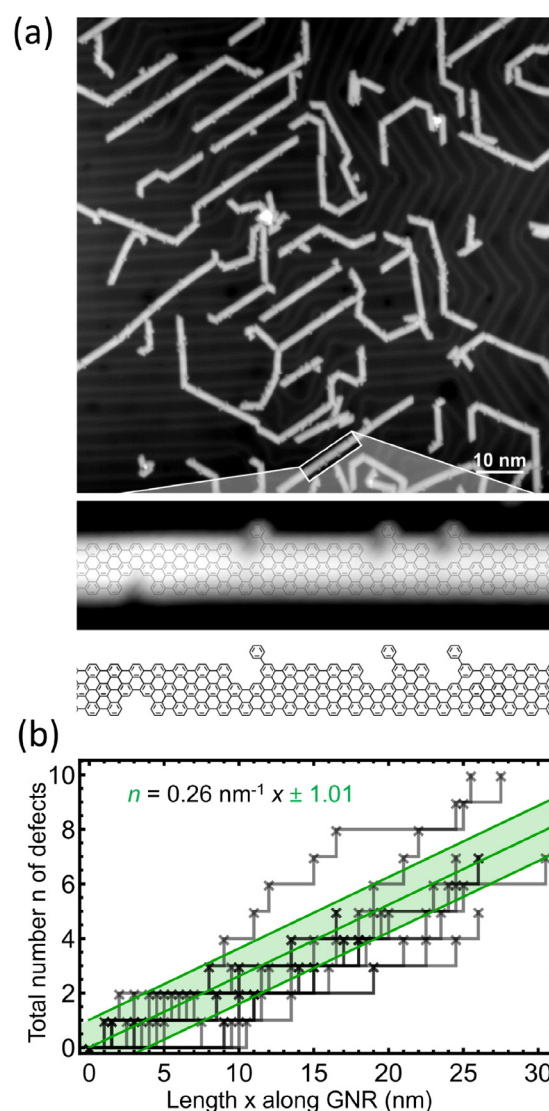
FIG. 5. STM characterization of the structural quality of 9-AGNRs. (a) STM topographic image of a 9-AGNR sample grown at lower coverage on Au(111) substrates ($V = 500$ mV, $I = 50$ pA). The 9-AGNRs are grown at lower density to facilitate high-resolution imaging. Note that the quality and length profile of the GNRs at lower density may differ from those at high coverage, which tend to be of higher quality and longer length. The devices were made with the high-coverage samples. The inset provides a closer view of the defects in the GNR structure, which are bite defects characterized by missing benzene rings at the edges. (b) The cumulative distribution of edge defects along the length of the GNRs shows the total number of bite defects as a function of length across all GNRs. A linear fit to the data reveals that the defect density is approximately one defect per 4 nm of the GNRs, so a GNR spanning a channel with length of 20 nm will have an average of five defects.

III. CONCLUSION

In conclusion, we thoroughly examined the effects of different metal depositions on the structure and charge transport of 9-AGNRs. Our detailed Raman spectroscopy measurements and absorption calculations revealed that In deposition caused fewer structural

disruptions at the metal–GNR interface compared to Pd deposition. Unfortunately, we were unable to precisely determine the extent and characteristics of these disruptions within the interface. This difficulty arises from the challenge of directly visualizing the metal–GNR interface using conventional electron microscopy techniques, mainly due to the thinness and sensitivity of GNRs to electron beam-induced damage. Despite this limitation, our findings offer valuable insights into how contact metal deposition influences the structural properties of GNRs, which is essential for advancing high-performance GNR-based devices. Furthermore, we performed extensive electrical measurements and a comprehensive comparison of Pd and In contact devices. We found that certain key device characteristics, including device-to-device variation, on/off ratio, and SS, improved with In contacts. However, a significant improvement in the on-state current was not observed. To understand why the interface improvement did not result in a noticeable on-state current improvement, we studied individual GNRs and found the presence of edge defects in the GNR structure. Such edge defects might adversely affect charge transport, hindering the realization of their theoretically estimated electrical properties. This highlights the importance of directing efforts toward enhancing the quality of the GNR channel to fully capitalize on the potential benefits offered by In contacts. We believe that our study contributes to a better understanding of the factors influencing device performance and can guide future research in this area.

IV. METHODS

Growth and STM imaging of 9-AGNRs: Au(111)/mica (Phasis, Switzerland) was cleaned by two cycles of sputtering at $1\,kV\ Ar^+$ (10 min) and annealing at $470\,°C$ (10 min) in UHV. The 9-AGNR precursor monomer $3',6'$-di-iodine-$1,1':2',1''$-terphenyl (DITP) was sublimated onto the clean Au(111) from a quartz crucible heated to $70\,°C$ with the substrate at room temperature. After a deposition of a full monolayer, the substrate was heated to $200\,°C$ (0.5 K/s, 10 min) to initiate DITP polymerization, followed by annealing at $400\,°C$ (0.5 K/s, 10 min) to form the final GNR topology by cyclodehydrogenation. STM images of 9-AGNRs on Au(111)/mica were acquired at room temperature using a Scienta Omicron VT-STM. Topographic images were acquired in constant current mode using a sample bias of $-1.5\,V$ and a setpoint current of 30 pA.

Transfer of 9-AGNRs: The transfer of 9-AGNRs was done by using the polymer-free method, with the following steps: (I) GNR/Au (111)/mica samples are floated on aqueous HCl solution until mica cleaves off from the Au film, (II) ultra-pure water is added to substantially reduce the HCl concentration, (III) pick up of GNR/Au with target substrate, (IV) drop of ethanol and annealing to increase Au adhesion to the target substrate, and (V) etching the Au layer. For more details on the transfer, see Refs. 38 and 67.

Raman spectroscopy characterization: Raman spectroscopy was performed using a Horiba Jobin Yvon LabRAM ARAMIS Raman microscope using a 785 nm laser with <10 mW power and a $100\times$ objective lens, resulting in a laser spot size of $<1\,\mu m$. No thermal effects were observed under these measurement conditions, and at least ten spectra from different points were collected for each sample.

Absorption calculations: The wavelength of the incoming laser radiation is considered to be 785 nm, and it is entering in an orthogonal direction to the film surface. Then, we calculate the normalized absorbed laser fluence based on the transfer matrix calculation, considering the thickness and optical constants of the individual layers.

By calculating the area under the curve for HfO_2 (5 nm) layer, for the three structures, we compare the absorbed laser fluence in these structures (assuming the GNR is mostly sensitive to the light absorbed by the material beneath that).[56]

Device fabrication: After the transfer, poly(methyl methacrylate) (molecular weight 950 kDa) was spun on the chips at 4000 rpm followed by a 10 min bake at $180\,°C$. Next, the S and D electrodes were patterned using a JEOL 6300-FS 100 kV EBL system and subsequently developed in 3:1 IPA-MIBK at $5\,°C$ for 90 s. Finally, $\sim$8 nm of In was deposited, followed by $\sim$20 nm Au deposition using e-beam evaporation under $\sim10^{-8}$ Torr, and liftoff was completed in a Remover PG at $80\,°C$. Fabrication details of the devices with Pd contacts can be found in our recent publications.[18,70]

Transport measurements: Transport measurements were conducted using the Lakeshore CPX-HF probe and the Agilent 4155C semiconductor parameter analyzer, controlled by the EasyEXPERT software, and the Lakeshore TTPX probe station, controlled by M81-SSM Synchronous Source Measure. The measurements took place at room temperature under a vacuum condition of 1×10^{-5} Torr.

STM imaging and analysis of edge defects: STM experiments were performed using a commercial CreaTec LT-STM operating at $T = 4\,K$ using Pt/Ir STM tips. Image processing of the STM scans was performed using WSxM software[68] and Mathematica.[69]

AUTHOR DECLARATIONS
Conflict of Interest

The authors have no conflicts to disclose.

Author Contributions

Zafer Mutlu: Conceptualization (lead); Investigation (lead); Project administration (lead); Resources (lead); Supervision (lead); Writing – original draft (lead); Writing – review & editing (lead). **Christina Dinh:** Writing – original draft (equal); Writing – review & editing (equal). **Gabriela Borin Barin:** Investigation (equal); Methodology (equal); Validation (equal); Visualization (equal); Writing – original draft (equal); Writing – review & editing (equal). **Peter H. Jacobse:** Investigation (equal); Methodology (equal); Validation (equal); Visualization (equal); Writing – original draft (equal); Writing – review & editing (equal). **Aravindh Kumar:** Investigation (supporting); Methodology (supporting); Writing – review & editing (supporting). **Debanjan Polley:** Data curation (supporting); Formal analysis (supporting); Investigation (supporting); Visualization (supporting); Writing – original draft (supporting); Writing – review & editing (supporting). **Hanuman Singh:** Investigation (supporting); Writing – review & editing (supporting). **Ziyi Wang:** Investigation (supporting); Writing – review & editing (supporting). **Yuxuan Cosmi Lin:** Data curation (equal); Formal analysis (equal); Investigation (equal); Methodology (equal); Validation (equal); Writing – review & editing (supporting). **Adam Michael Schwartzberg:** Investigation (supporting); Methodology (supporting); Resources (supporting); Writing – review & editing (supporting). **Michael F. Crommie:** Funding acquisition (supporting); Investigation (supporting); Resources (supporting); Writing – review & editing (supporting). **Klaus Mullen:** Investigation (supporting); Resources (supporting); Writing – review & editing (supporting). **Pascal Ruffieux:** Investigation (supporting); Writing – review & editing (supporting). **Roman Fasel:** Funding acquisition (supporting); Investigation (supporting); Methodology (supporting); Resources (supporting); Visualization (supporting); Writing – review & editing (supporting). **Jeffrey Bokor:** Funding acquisition (supporting); Project administration (equal); Resources (equal); Supervision (equal); Writing – review & editing (supporting).

DATA AVAILABILITY

The data that support the findings of this study are available from the corresponding author upon reasonable request.

REFERENCES

[1]G. Moore, *The Future of Integrated Electronics* (Fairchild Semiconductor Internal Publication, 1964).

[2]A. D. Franklin, M. C. Hersam, and H.-S. P. Wong, "Carbon nanotube transistors: Making electronics from molecules," Science **378**, 726–732 (2022).

[3]J. Cai, P. Ruffieux, R. Jaafar, M. Bieri, T. Braun, S. Blankenburg, M. Muoth, A. P. Seitsonen, M. Saleh, X. Feng *et al.*, "Atomically precise bottom-up fabrication of graphene nanoribbons," Nature **466**, 470–473 (2010).

[4]L. Chen, L. Wang, and D. Beljonne, "Designing coved graphene nanoribbons with charge carrier mobility approaching that of graphene," Carbon **77**, 868–879 (2014).

[5]Z. Mutlu, Y. Lin, G. Barin, Z. Zhang, G. Pitner, S. Wang, R. Darawish, M. Di Giovannantonio, H. Wang, J. Cai *et al.*, "Short-channel double-gate fets with atomically precise graphene nanoribbons," in *IEEE International Electron Devices Meeting (IEDM)* (IEEE, 2021).

[6]Y.-W. Son, M. L. Cohen, and S. G. Louie, "Energy gaps in graphene nanoribbons," Phys. Rev. Lett. **97**, 216803 (2006).

[7]L. Yang, C.-H. Park, Y.-W. Son, M. L. Cohen, and S. G. Louie, "Quasiparticle energies and band gaps in graphene nanoribbons," Phys. Rev. Lett. **99**, 186801 (2007).

[8]P. B. Bennett, Z. Pedramrazi, A. Madani, Y.-C. Chen, D. G. de Oteyza, C. Chen, F. R. Fischer, M. F. Crommie, and J. Bokor, "Bottom-up graphene nanoribbon field-effect transistors," Appl. Phys. Lett. **103**, 253114 (2013).

[9]J. P. Llinas, A. Fairbrother, G. Borin Barin, W. Shi, K. Lee, S. Wu, B. Yong Choi, R. Braganza, J. Lear, N. Kau *et al.*, "Short-channel field-effect transistors with 9-atom and 13-atom wide graphene nanoribbons," Nat. Commun. **8**, 633 (2017).

[10]C. Hsu, M. Rohde, G. Borin Barin, G. Gandus, D. Passerone, M. Luisier, P. Ruffieux, R. Fasel, H. S. van der Zant, and M. E. Abbassi, "Platinum contacts for 9-atom-wide armchair graphene nanoribbons," Appl. Phys. Lett. **122**, 173104 (2023).

[11]D. Bouwmeester, T. S. Ghiasi, G. B. Barin, K. Müllen, P. Ruffieux, R. Fasel, and H. S. van der Zant, "More electrodes with 10-nm nanogaps for electrical contact to atomically precise graphene nanoribbons," arXiv:2306.16070 (2023).

[12]O. Braun, J. Overbeck, M. El Abbassi, S. Käser, R. Furrer, A. Olziersky, A. Flasby, G. B. Barin, Q. Sun, R. Darawish *et al.*, "Optimized graphene electrodes for contacting graphene nanoribbons," Carbon **184**, 331–339 (2021).

[13]L. Martini, Z. Chen, N. Mishra, G. B. Barin, P. Fantuzzi, P. Ruffieux, R. Fasel, X. Feng, A. Narita, C. Coletti *et al.*, "Structure-dependent electrical properties of graphene nanoribbon devices with graphene electrodes," Carbon **146**, 36–43 (2019).

[14]Z. Mutlu and J. Bokor, "Bottom-up synthesized graphene nanoribbon transistors," in *6th IEEE Electron Devices Technology & Manufacturing Conference (EDTM)* (IEEE, 2022), pp. 157–159.

[15]V. Passi, A. Gahoi, B. V. Senkovskiy, D. Haberer, F. R. Fischer, A. Gruuneis, and M. C. Lemme, "Field-effect transistors based on networks of highly aligned, chemically synthesized $N = 7$ armchair graphene nanoribbons," ACS Appl. Mater. Interfaces **10**, 9900–9903 (2018).

[16]M. Ohtomo, Y. Sekine, H. Hibino, and H. Yamamoto, "Graphene nanoribbon field-effect transistors fabricated by etchant-free transfer from Au (788)," Appl. Phys. Lett. **112**, 021602 (2018).

[17]Z. Mutlu, P. H. Jacobse, R. D. McCurdy, J. P. Llinas, Y. Lin, G. C. Veber, F. R. Fischer, M. F. Crommie, and J. Bokor, "Bottom-up synthesized nanoporous graphene transistors," Adv. Funct. Mater. **31**, 2103798 (2021).

[18]Y. C. Lin, Z. Mutlu, G. B. Barin, Y. Hong, J. P. Llinas, A. Narita, H. Singh, K. Müllen, P. Ruffieux, R. Fasel *et al.*, "Scaling and statistics of bottom-up synthesized armchair graphene nanoribbon transistors," Carbon **205**, 519–526 (2023).

[19]G. Borin Barin, Q. Sun, M. Di Giovannantonio, C.-Z. Du, X.-Y. Wang, J. P. Llinas, Z. Mutlu, Y. Lin, J. Wilhelm, J. Overbeck *et al.*, "Growth optimization and device integration of narrow-bandgap graphene nanoribbons," Small **18**, 2202301 (2022).

[20]G. Pitner, G. Hills, J. P. Llinas, K.-M. Persson, R. Park, J. Bokor, S. Mitra, and H.-S. P. Wong, "Low-temperature side contact to carbon nanotube transistors: Resistance distributions down to 10 nm contact length," Nano Lett. **19**, 1083–1089 (2019).

[21]A. Javey, J. Guo, M. Paulsson, Q. Wang, D. Mann, M. Lundstrom, and H. Dai, "High-field quasiballistic transport in short carbon nanotubes," Phys. Rev. Lett. **92**, 106804 (2004).

[22]B.-K. Kim, T.-H. Kim, D.-H. Choi, H. Kim, K. Watanabe, T. Taniguchi, H. Rho, J.-J. Kim, Y.-H. Kim, and M.-H. Bae, "Origins of genuine ohmic van der Waals contact between indium and MoS_2," npj 2D Mater. Appl. **5**, 9 (2021).

[23]A. Kumar, K. Schauble, K. M. Neilson, A. Tang, P. Ramesh, H.-S. P. Wong, E. Pop, and K. Saraswat, "Sub-200 $\Omega \cdot \mu m$ alloyed contacts to synthetic monolayer MoS_2," in *IEEE International Electron Devices Meeting (IEDM)* (IEEE, 2021).

[24]Y. Wang, J. C. Kim, R. J. Wu, J. Martinez, X. Song, J. Yang, F. Zhao, A. Mkhoyan, H. Y. Jeong, and M. Chhowalla, "Van der Waals contacts between three-dimensional metals and two-dimensional semiconductors," Nature **568**, 70–74 (2019).

[25]L. Talirz, H. Sode, T. Dumslaff, S. Wang, J. R. Sanchez-Valencia, J. Liu, P. Shinde, C. A. Pignedoli, L. Liang, V. Meunier *et al.*, "On-surface synthesis and characterization of 9-atom wide armchair graphene nanoribbons," ACS Nano **11**, 1380–1388 (2017).

[26]M. Di Giovannantonio, O. Deniz, J. I. Urgel, R. Widmer, T. Dienel, S. Stolz, C. Sánchez-Sánchez, M. Muntwiler, T. Dumslaff, R. Berger *et al.*, "On-surface growth dynamics of graphene nanoribbons: The role of halogen functionalization," ACS Nano **12**, 74–81 (2018).

24 October 2024 08:40:46

[27]L. Talirz, P. Ruffieux, and R. Fasel, "On-surface synthesis of atomically precise graphene nanoribbons," Adv. Mater. **28**, 6222–6231 (2016).

[28]Z. Chen, A. Narita, and K. Müllen, "Graphene nanoribbons: On-surface synthesis and integration into electronic devices," Adv. Mater. **32**, 2001893 (2020).

[29]Y. Gu, Z. Qiu, and K. Mullen, "Nanographenes and graphene nanoribbons as multitalents of present and future materials science," J. Am. Chem. Soc. **144**, 11499–11524 (2022).

[30]R. K. Houtsma, J. de la Rie, and M. Stöhr, "Atomically precise graphene nanoribbons: Interplay of structural and electronic properties," Chem. Soc. Rev. **50**, 6541–6568 (2021).

[31]F. Schulz, P. H. Jacobse, F. F. Canova, J. Van Der Lit, D. Z. Gao, A. Van Den Hoogenband, P. Han, R. J. Klein Gebbink, M.-E. Moret, P. M. Joensuu et al., "Precursor geometry determines the growth mechanism in graphene nanoribbons," J. Phys. Chem. C **121**, 2896–2904 (2017).

[32]P. H. Jacobse, R. D. McCurdy, J. Jiang, D. J. Rizzo, G. Veber, P. Butler, R. Zuzak, S. G. Louie, F. R. Fischer, and M. F. Crommie, "Bottom-up assembly of nanoporous graphene with emergent electronic states," J. Am. Chem. Soc. **142**, 13507–13514 (2020).

[33]P. H. Jacobse, K. A. Simonov, M. J. Mangnus, G. I. Svirskiy, A. V. Generalov, A. S. Vinogradov, A. Sandell, N. Mårtensson, A. B. Preobrajenski, and I. Swart, "One precursor but two types of graphene nanoribbons: On-surface transformations of 10,10′-dichloro-9, 9′-bianthryl on Ag (111)," J. Phys. Chem. C **123**, 8892–8901 (2019).

[34]D. J. Rizzo, J. Jiang, D. Joshi, G. Veber, C. Bronner, R. A. Durr, P. H. Jacobse, T. Cao, A. Kalayjian, H. Rodriguez et al., "Rationally designed topological quantum dots in bottom-up graphene nanoribbons," ACS Nano **15**, 20633–20642 (2021).

[35]P. H. Jacobse, Z. Jin, J. Jiang, S. Peurifoy, Z. Yue, Z. Wang, D. J. Rizzo, S. G. Louie, C. Nuckolls, and M. F. Crommie, "Pseudo-atomic orbital behavior in graphene nanoribbons with four-membered rings," Sci. Adv. **7**, eabl5892 (2021).

[36]E. C. H. Wen, P. H. Jacobse, J. Jiang, Z. Wang, R. D. McCurdy, S. G. Louie, M. F. Crommie, and F. R. Fischer, "Magnetic interactions in substitutional core-doped graphene nanoribbons," J. Am. Chem. Soc. **144**, 13696–13703 (2022).

[37]J. Yin, P. H. Jacobse, D. Pyle, Z. Wang, M. F. Crommie, and G. Dong, "Programmable fabrication of monodisperse graphene nanoribbons via deterministic iterative synthesis," J. Am. Chem. Soc. **144**, 16012–16019 (2022).

[38]G. Borin Barin, A. Fairbrother, L. Rotach, M. Bayle, M. Paillet, L. Liang, V. Meunier, R. Hauert, T. Dumslaff, A. Narita et al., "Surface-synthesized graphene nanoribbons for room temperature switching devices: Substrate transfer and ex situ characterization," ACS Appl. Nano Mater. **2**, 2184–2192 (2019).

[39]O. Deniz, C. Sánchez-Sánchez, T. Dumslaff, X. Feng, A. Narita, K. Mullen, N. Kharche, V. Meunier, R. Fasel, and P. Ruffieux, "Revealing the electronic structure of silicon intercalated armchair graphene nanoribbons by scanning tunneling spectroscopy," Nano Lett. **17**, 2197–2203 (2017).

[40]J. Overbeck, G. Borin Barin, C. Daniels, M. L. Perrin, L. Liang, O. Braun, R. Darawish, B. Burkhardt, T. Dumslaff, X.-Y. Wang et al., "Optimized substrates and measurement approaches for Raman spectroscopy of graphene nanoribbons," Phys. Status Solidi B **256**, 1900343 (2019).

[41]S. Zhao, G. B. Barin, T. Cao, J. Overbeck, R. Darawish, T. Lyu, S. Drapcho, S. Wang, T. Dumslaff, A. Narita et al., "Optical imaging and spectroscopy of atomically precise armchair graphene nanoribbons," Nano Lett. **20**, 1124–1130 (2020).

[42]B. Senkovskiy, M. Pfeiffer, S. Alavi, A. Bliesener, J. Zhu, S. Michel, A. Fedorov, R. German, D. Hertel, D. Haberer et al., "Making graphene nanoribbons photoluminescent," Nano Lett. **17**, 4029–4037 (2017).

[43]H. Huang, D. Wei, J. Sun, S. L. Wong, Y. P. Feng, A. C. Neto, and A. T. S. Wee, "Spatially resolved electronic structures of atomically precise armchair graphene nanoribbons," Sci. Rep. **2**, 983 (2012).

[44]B. V. Senkovskiy, A. V. Fedorov, D. Haberer, M. Farjam, K. A. Simonov, A. B. Preobrajenski, N. Mårtensson, N. Atodiresei, V. Caciuc, S. Blügel et al., "Semiconductor-to-metal transition and quasiparticle renormalization in doped graphene nanoribbons," Adv. Electron. Mater. **3**, 1600490 (2017).

[45]A. C. Ferrari and D. M. Basko, "Raman spectroscopy as a versatile tool for studying the properties of graphene," Nat. Nanotechnol. **8**, 235–246 (2013).

[46]M. Yamada, Y. Yamakita, and K. Ohno, "Phonon dispersions of hydrogenated and dehydrogenated carbon nanoribbons," Phys. Rev. B **77**, 054302 (2008).

[47]R. Gillen, M. Mohr, C. Thomsen, and J. Maultzsch, "Vibrational properties of graphene nanoribbons by first-principles calculations," Phys. Rev. B **80**, 155418 (2009).

[48]M. S. Dresselhaus, G. Dresselhaus, R. Saito, and A. Jorio, "Raman spectroscopy of carbon nanotubes," Phys. Rep. **409**, 47–99 (2005).

[49]C. Ma, L. Liang, Z. Xiao, A. A. Puretzky, K. Hong, W. Lu, V. Meunier, J. Bernholc, and A.-P. Li, "Seamless staircase electrical contact to semiconducting graphene nanoribbons," Nano Lett. **17**, 6241–6247 (2017).

[50]J. Zhou and J. Dong, "Vibrational property and raman spectrum of carbon nanoribbon," Appl. Phys. Lett. **91**, 173108 (2007).

[51]A. Fairbrother, J.-R. Sanchez-Valencia, B. Lauber, I. Shorubalko, P. Ruffieux, T. Hintermann, and R. Fasel, "High vacuum synthesis and ambient stability of bottom-up graphene nanoribbons," Nanoscale **9**, 2785–2792 (2017).

[52]C. Ma, Z. Xiao, A. A. Puretzky, A. P. Baddorf, W. Lu, K. Hong, J. Bernholc, and A.-P. Li, "Oxidization stability of atomically precise graphene nanoribbons," Phys. Rev. Mater. **2**, 014006 (2018).

[53]R. Honig and D. Kramer, *Vapor Pressure Data for the Solid and Liquid Elements* (RCA Laboratories, 1969).

[54]C. Archambault and A. Rochefort, "States modulation in graphene nanoribbons through metal contacts," ACS Nano **7**, 5414–5420 (2013).

[55]T. Nikitin, S. Novikov, and L. Khriachtchev, "Giant raman gain in annealed silicon-rich silicon oxide films: Measurements at 785 nm," Appl. Phys. Lett. **103**, 151110 (2013).

[56]L. Alber, V. Scalera, V. Unikandanunni, D. Schick, and S. Bonetti, "Ntmpy: An open source package for solving coupled parabolic differential equations in the framework of the three-temperature model," Comput. Phys. Commun. **265**, 107990 (2021).

[57]J. Chatterjee, D. Polley, A. Pattabi, H. Jang, S. Salahuddin, and J. Bokor, "RKKY exchange bias mediated ultrafast all-optical switching of a ferromagnet," Adv. Funct. Mater. **32**, 2107490 (2022).

[58]F. R. Fischer, J. Bokor, Z. Mutlu, J. P. Llinas, R. D. Mccurdy, G. C. Veber, and D. J. Koenigs, "Low band gap graphene nanoribbon electronic devices," US patent 17/608,355 (2022).

[59]I. M. Datye, A. J. Gabourie, C. D. English, K. K. Smithe, C. J. McClellan, N. C. Wang, and E. Pop, "Reduction of hysteresis in MoS_2 transistors using pulsed voltage measurements," 2D Mater. **6**, 011004 (2018).

[60]K. K. Smithe, S. V. Suryavanshi, M. Muñoz Rojo, A. D. Tedjarati, and E. Pop, "Low variability in synthetic monolayer MoS_2 devices," ACS Nano **11**, 8456–8463 (2017).

[61]Y. Y. Illarionov, K. K. Smithe, M. Waltl, T. Knobloch, E. Pop, and T. Grasser, "Improved hysteresis and reliability of MoS_2 transistors with high-quality CVD growth and Al_2O_3 encapsulation," IEEE Electron Device Lett. **38**, 1763–1766 (2017).

[62]M. Pizzochero, K. Čerņevičs, G. B. Barin, S. Wang, P. Ruffieux, R. Fasel, and O. V. Yazyev, "Quantum electronic transport across 'bite' defects in graphene nanoribbons," 2D Mater. **8**, 035025 (2021).

[63]M. Pizzochero, G. B. Barin, K. Cernevics, S. Wang, P. Ruffieux, R. Fasel, and O. V. Yazyev, "Edge disorder in bottom-up zigzag graphene nanoribbons: Implications for magnetism and quantum electronic transport," J. Phys. Chem. Lett. **12**, 4692–4696 (2021).

[64]S. Jiang, F. Scheurer, Q. Sun, P. Ruffieux, X. Yao, A. Narita, K. Mullen, R. Fasel, T. Frederiksen, and G. Schull, "Length-independent quantum transport through topological band states of graphene nanoribbons," arXiv:2208.03145 (2022).

[65]Q. Sun, O. Gröning, J. Overbeck, O. Braun, M. L. Perrin, G. Borin Barin, M. El Abbassi, K. Eimre, E. Ditler, C. Daniels et al., "Massive Dirac fermion behavior in a low bandgap graphene nanoribbon near a topological phase boundary," Adv. Mater. **32**, 1906054 (2020).

[66]J. Yamaguchi, H. Hayashi, H. Jippo, A. Shiotari, M. Ohtomo, M. Sakakura, N. Hieda, N. Aratani, M. Ohfuchi, Y. Sugimoto et al., "Small bandgap in atomically precise 17-atom-wide armchair-edged graphene nanoribbons," Commun. Mater. **1**, 36 (2020).

[67]C. Backes, A. M. Abdelkader, C. Alonso, A. Andrieux-Ledier, R. Arenal, J. Azpeitia, N. Balakrishnan, L. Banszerus, J. Barjon, R. Bartali et al.,

"Production and processing of graphene and related materials," 2D Mater. **7**, 022001 (2020).

[68]I. Horcas, R. Fernández, J. Gomez-Rodriguez, J. Colchero, J. Gómez-Herrero, and A. Baro, "Wsxm: A software for scanning probe microscopy and a tool for nanotechnology," Rev. Sci. Instrum. **78**, 013705 (2007).

[69]P. H. Jacobse, "MathemaTB: A *Mathematica* package for tight-binding calculations," Comput. Phys. Commun. **244**, 392–408 (2019).

[70]Z. Mutlu, J. P. Llinas, P. H. Jacobse, I. Piskun, R. Blackwell, M. F. Crommie, F. R. Fischer, and J. Bokor, "Transfer-free synthesis of atomically precise graphene nanoribbons on insulating substrates," ACS Nano **15**, 2635–2642 (2021).

24 October 2024 08:40:46